ORIGINAL RESEARCH

The bending dependency of forming limit diagrams

Felix M. Neuhauser[1] · Oscar Terrazas[2] · Niko Manopulo[1] · Pavel Hora[1] · Chester Van Tyne[2]

Abstract

The forming limit diagram (FLD) is commonly used in the forming industry to predict localized necking in sheet metals. However, experimental and mathematical determination of forming limit curves is based on in-plane deformation without taking a bending component into account. This paper addresses the question whether a forming limit diagram predicts localized necking too conservatively or too liberally for different amounts of superimposed bending. Furthermore a methodology is proposed on how to determine the influence of bending quantitatively and how to incorporate the results into a FLD. Finite element analysis (FEA) is used to model the angular stretch bend test (ASBT), where a strip of sheet metal is locked at both ends and a tool with a radius stretches and bends the center of the strip until failure. By using different radii, the sample is exposed to different amounts of superimposed bending during the stretching. The FEA model is verified by experimental work using a dual phase steel (DP600). Applying a strain rate dependent identification method for determining the onset of localized necking, the FEA model is utilized to access the forming limit strains for different stretch bending conditions. Thereby the Keeler-Brazier FLD is extended by a third dimension, the superimposed bending dimension, to assess the effect of bending on the forming limit of sheet metal parts. The more severe the superimposed bending, the higher the formability of the steel.

Introduction

During deep drawing processes, a sheet of metal is pulled off of a binder by the punch into the cavity of a die. Strains will appear, which are not only in the plane of the sheet and strain gradients evolve throughout the sheet's thickness. This happens in modern car body production, e.g., when material is stretched over sharp contours and edges. However, the overall failure assessment of the sheet is based on conventional forming limit diagrams, which in turn are either experimentally determined, such as by Marciniak tests, or theoretically determined, e.g. with the modified maximum force critrion and only consider in-plane deformation (i.e. pure stretching but no bending) [1, 2]. Meanwhile, it is well known that out-of-plane deformation like bending enhances the formability of sheet steel. Tharett and Stoughton found that for mild to severe amounts of superimposed bending to stretching of 1008 AK steels, the neck of the sheet will form on a convex surface when the strain on the concave side of the sheet reaches the forming limit in plane-strain for in-plane deformation. This rule is referred to as the concave-side rule (CSR) [3]. Kitting et al. conducted experimental angular stretch bend tests (ASBTs) on H340LAD micro-alloyed steel to assess the predictive quality of the CSR for uniaxial to plane-strain deformation paths. They found that for mild superimposed bending, the CSR is valid, but that this measure loses accuracy for more pronounced inhomogeneous through-thickness deformation [4]. Similarly, Neuhauser et al. performed a series of experimental and simulative ASBTs of different DP steel grades and found

✉ Chester Van Tyne
cvantyne@mines.edu

Felix M. Neuhauser
neuhauser@ivp.mavt.ethz.ch

[1] Institute of Virtual Manufacturing, Department of Mechanical and Process Engineering, Swiss Federal Institute of Technology, Tannenstrasse 3, 8092 Zurich, Switzerland

[2] Advanced Steel Processing and Products Research Center, Colorado School of Mines, 920 15th St, Golden, CO 80401 USA

that the CSR applies only to severe superimposed bending and is therefore not universally applicable [5]. Since the ASBT is limited to the characterization of stretch-bending for strain paths only from uniaxial to plane strain, Kitting et al. have introduced a novel stretch-bending test setup to assess stretch-bending forming limits in biaxial stretching conditions. It was found that for biaxial strain path with superimposed bending, the formability also increases [6, 7]. Levy and Van Tyne determined the applied stress on a bend that caused breakage for ASBTs with different radii and for various sheet thicknesses and dual-phase high strength steels. The ratio of the failure stress to Stoughton's stress-based forming limit stress is defined as the failure stress ratio, and is correlated to the ratio of thickness to radius in developing predictive equations for failure that is due to bending. They observed linear relationships, where for increased bending, the failure stress ratio decreases throughout the different steel grades [8]. De Kruijf et al. performed FEA of a simplified test sample that is subject to bending with subsequent stretching, stretching with subsequent bending, and stretching with simultaneous bending. In the case of the stretch-bending no necking could be observed while when prebending is applied, neck initiation is accelerated by the bending. For simultaneous stretching and bending, the initiation of necking was found to be considerably delayed [9]. Theoretical formulations for bending-enhanced FLD have been proposed by Xia et al. where the theory of plasticity is also used to predict sheet metal behavior in terms of radius over thickness ratios. Their derivations show a clear enhancement of formability by bending and are consistent with experimental observations [10]. Vallellano et al. accounted for the strain gradient through the thickness of the material by means of a simplification of the stretch bending process through a two-step bilinear model. A combination of the CSR and a critical-distance methodology was emphasized to account for the two types of failures that occur during stretch-bending: a necking-controlled failure, which occurs when stretching dominates the fibers in the sheet and becomes plastically unstable, and a fracture-controlled ductile failure, which arises when bending dominates and cracks initiate in the convex fibers of the sheet [11]. Morales-Palma et al. developed a two-step deformation model that permits a description of the compression-tension process that occurs in the material on the inner side of the sheet. Their failure criterion suggests that the material on the concave side of the bend is responsible for necking, but that ductile fracture is controlled by the material on the convex side. Therefore, when tension dominates over bending, failure due to necking is more likely, and when the stress gradient prevails throughout the thickness, failure by ductile fracture will occur on the convex side of the surface and will propagate through the thickness [12]. Hora et al. also consider the influence of curvature

along with thickness on the FLD in the enhanced modified maximum force criterion [13].

The current study presents the results of an experimentally verified FEA of an ASBT, where localized necking strains are identified through the time-dependent method proposed by Volk and Hora [14]. A total of 14 different radii are used to set the sheet under tension with mild to severe superimposed bending. Using the forming limits in plane strain for different thickness over radius ratios, the Keeler-Brazier FLD is extended to a third bending dimension.

Constitutive model

The current study used a DP600 steel to analyze the effect of bending on the forming limit curve.

Flow curve Four tensile tests were performed in the rolling direction at a strain rate of $\dot{\epsilon}_0 = 0.002 \frac{1}{s}$ in order to determine the material's static stress response. A mixed Hockett-Sherby/Gosh hardening law was fit to the data and was used to extrapolate the measured stress response of the material.

$$\sigma_{HS} = A_1 - (A_1 - B_1)\exp(-m_1\epsilon_{pl}^{n_1}) \tag{1}$$

$$\sigma_G = A_2(B_2 + \epsilon_{pl})^{n_2} - C_2 \tag{2}$$

$$\sigma_{HS,G} = \kappa\sigma_{HS} + (1 - \kappa)\sigma_G \tag{3}$$

The combination factor of $\kappa = 0.85$ was chosen so that the slope of the experimental hardening curve is precisely matched at the truncation of the experimental stress-strain curve to ensure a reasonable extrapolation beyond the uniform elongation. The flow curves are shown in Fig. 1,
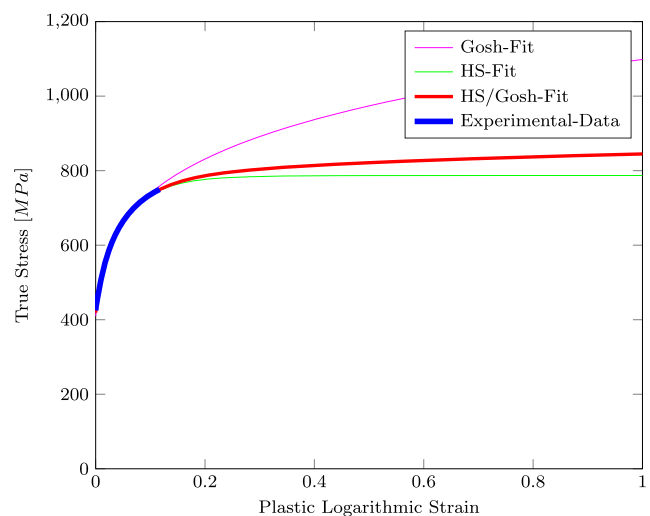

Fig. 1 Mixed Hockett-Sherby Gosh flow curve fitted to the experimental data

and the parameters for the material description are listed in Tables 1 and 2.

In order to capture the dependency of the flow curve on the strain rate, further tensile tests with increased strain rates were performed $(0.01\frac{1}{s}, 0.1\frac{1}{s}, 0.15\frac{1}{s})$, with three tensile tests conducted at each strain rate to ensure repeatability. Next, the strain-rate-dependent part of the Johnson-Cook model was fitted to the experimental data.

$$\sigma_{JC} = \sigma_{HS,G} \left(1 + C \ln \frac{\dot{\epsilon}_{pl}}{\dot{\epsilon}_0}\right) \quad (4)$$

Therefore, $\dot{\epsilon}_0$ is the strain rate used to determine the parameters for the strain hardening term. Capturing the effect of strain rate is important when accessing strains after a diffuse neck. Once strains begin to localize, strain rates increase drastically where the neck has formed. With a positive strain rate, strain distribution is homogenized, and as a result, the localization is delayed. However, only a small degree of strain-rate sensitivity could be detected with $C = 0.008$.

Yield locus The Hill 48 yield surface was used to model the anisotropy of the investigated DP600 sheet steel,

$$F(\sigma_{22} - \sigma_{33})^2 + G(\sigma_{33} - \sigma_{11})^2 + H(\sigma_{11} - \sigma_{22})^2 + ...$$
$$... + 2L\sigma_{23}^2 + 2M\sigma_{31}^2 + 2N\sigma_{12}^2 = (\sigma^0)^2 \quad (5)$$

where the parameters F, G, H, L, M, and N can all be determined using the yield-stress ratios $R_{11} = 1$, $R_{22} = \frac{\sigma_{22}^y}{\sigma^0}$, $R_{33} = \frac{\sigma_{33}^y}{\sigma^0}$, $R_{12} = \frac{\sigma_{12}^y}{\sigma^0}$, $R_{13} = \frac{\sigma_{13}^y}{\sigma^0}$, $R_{23} = \frac{\sigma_{23}^y}{\sigma^0}$ and σ^0 is the yield stress in the rolling direction. In sheet metal forming, it is common to find the anisotropy of the material in terms of Lankford's coefficients, since it is not possible to conduct tensile and shear tests in the thickness direction. The anisotropy coefficients measured at tensile test specimens cut in the 0°, 45° and 90° directions are shown in Table 3. They were measured at 10% elongation while the samples were still under load and clamped in the tensile frame. Again, three tensile tests for all three directions were conducted to ensure repeatability. Applying the flow rule enables the conversion of Lankford's coefficients to stress ratios. However, parameters R_{13} and R_{23}, which are related to out of plane shear, cannot be determined through simple tensile tests. As a result, they were assumed to be equal to R_{12} in this study. Figure 2 shows the form of the determined yield locus.

Table 1 Material parameters for the Hockett-Sherby hardening law

$A_{HS}[MPa]$	$B_{HS}[MPa]$	m_{HS}	n_{HS}
790.0	394.7	9.2	0.75

Table 2 Material parameters for the Gosh hardening law

$A_G[MPa]$	$B_G[MPa]$	n_G	$C_G[MPa]$
1049.2	0.0028	0.17	0

Hardening law and flow rule The hardening law was isotropic hardening. Although in stretch bending the bottom surface could be, depending on the amount of bending, subjected to initial compression, the kinematic hardening associated with the Bauschinger effect is neglected. For the flow rule, the associated flow rule was implemented.

Description of the angular stretch bend test

The purpose of the angular stretch bend test (ASBT) (see Fig. 3) is to subject a sheet steel to stretching with superimposed bending that is similar to the deformation state at both the die and punch radii in deep-drawing processes. The strain at the punch nose varies, depending on the lubrication condition and radius used, from strain paths that are close to uniaxial strain with high lubrication and near plane strain without lubrication. The tooling consists of a die, a holder, draw beads to lock the sheet, and a wedge-shaped punch with different radii to impose mild to severe bending. The sheet is clamped between the holder and the die, and the punch deforms the sheet until either fracture or a predefined load drop occurs. A sketch of the setup (see Fig. 4) and testing parameters are listed below:

- Tool geometry
    - Punch radii R_P: 2.5, 5.0, 7.5 and 10.0 mm
    - Die entry radius R_{DE}: 4.7 mm
    - Draw bead radius R_{DB}: 3.2 mm
    - Distance between draw beads D_{DB}: 95 mm
    - Die opening D_D: 76.2 mm
- Sheet steel samples:
    - Length: 180 mm
    - Width: 25 mm
    - Thickness: 1.45 mm
    - Material: DP600, machined by wire EDM
- Lubrication condition:
    - Teflon (PTFE)
    - LPS2 lubricant

Table 3 Lankford's coefficients for the DP600 steel

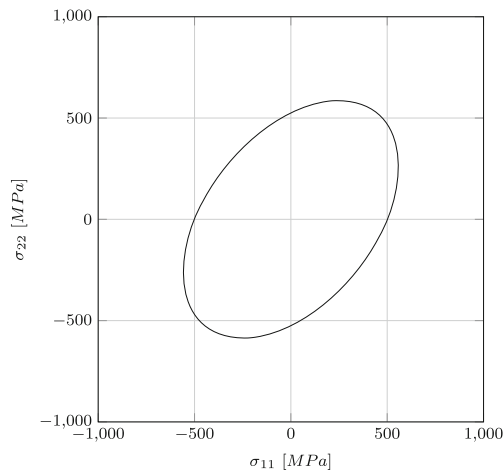| r_0	r_{45}	r_{90}
0.74	0.92	0.88

Fig. 2 Hill 48 yield locus in 2D space for a DP600 sheet steel

– Punch velocity:

  – 1.365 mm/s

Two types of fractures were observed: shear fracture at the top surface of the sheet steel at the location of the punch nose, and tensile fracture in the ligament (see Figs. 5 and 6). The smaller the amount of bending, the more likely the failure was to move to the unsupported ligaments where no bending is superimposed. Since the present study is interested in stretching with superimposed bending, samples that failed at the unsupported ligament were not analyzed further.

Finite element modeling

The general purpose software ABAQUS was used to model the angular stretch bend test. A three-dimensional model was implemented in which the tools (including the die, holder and punch) were represented by analytical rigid body surfaces. To extend the experimental campaign, punch radii of 2.0, 2.25, 2.5, 2.75, 3.0, 3.5, 4.0, 4.5, 5.0, 7.5, 10.0, 12.0,

Fig. 3 Setup of an angular stretch bend test. A 25 mm wide strip of DP600 sheet steel is gripped with a ligament length of 180 mm and deformed by a punch under constant displacement control
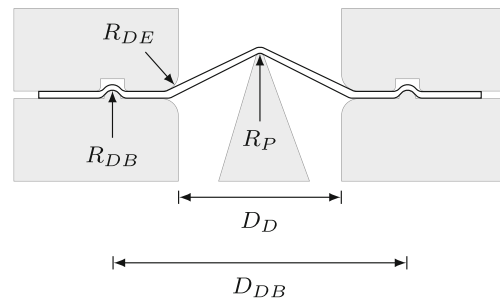

Fig. 4 Sketch of the ASBT

13.0, and 38 mm were used to model the deformation of the sheet. The blank was rendered by 3D linear 8-node brick elements with reduced integration to avoid locking. Fifteen elements were used through the thickness to account for the bending component. In the critical area (the blank at the punch nose), the mesh was refined. All model geometries matched their counterparts in the angular stretch bend test environment. Due to symmetry in both the blank length and width, only one-quarter of the total blank was modeled to save computational time. Another boundary condition was the fixing of the blank where the drawbead ends to lock the blank as a reasonable representation of the reality. The punch was displacement controlled, and the total displacement heights for radii 2.5, 5.0, 7.5, and 10.0 mm were determined from when failure occurred during the experiments. The punch velocity of 1.365 mm/s was used to match the experimental campaign. In order to ensure a high resolution of the strain states at the end of the analysis (which will be used for further processing), the maximum time increment was set to a small value of $\Delta t_{max} = 0.05 \ s$; in other words, 20 stress and strain states were evaluated per second. The friction coefficient was held constant between the holder and the sheet, as well as between the die and the sheet, at a value of 0.15. However, the friction coefficients between the punch and the sheet were determined by an inverse optimization in terms of force displacement curves for punch radii of 2.5, 5.0, 7.5, and 10.0 mm
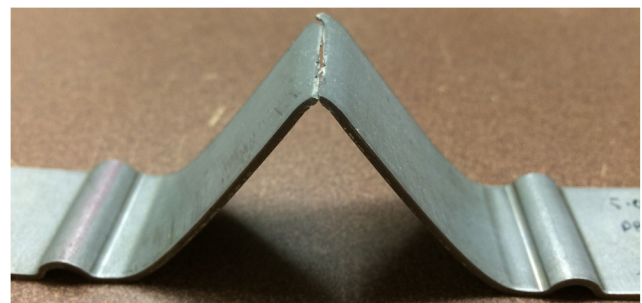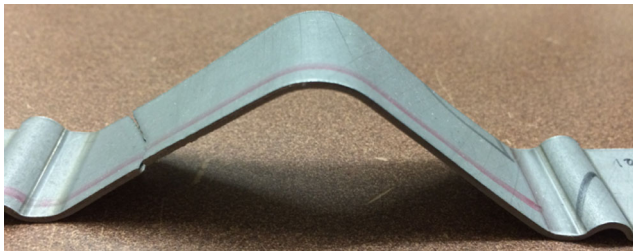

Fig. 5 Shear fracture at the punch nose

Fig. 6 Tensile fracture at the ligament

where experimental data were available. The remaining friction coefficients for the extra simulated punch radii were assumed to be the average friction coefficient of the four inversely optimized coefficients. Table 4 summarizes the information on elements, contact algorithms, friction coefficients, punch velocity, time increments, and material models used for modeling.

Verification of finite element and plasticity model

The finite element model was verified in two different ways. The first verification was in terms of comparing experimental and simulation force displacement curves of the punch, while the second verification was in terms of thickness measurements along the neck of the sample.

Table 4 Summarized Information on the Finite Element Model

Element type (ABAQUS)	C3D8R, Hourglass control
Mesh size (critical area)	$0.092\ mm \times 0.312\ mm \times 0.097\ mm$
Total number of elements	120 000
Integration points through thickness	15
Solver	ABAQUS Standard (implicit)
Contact algorithm	Penalty contact method
μ between holder/die and blank	$\mu = 0.15$
μ between punch and blank	$R = 2.5\ mm : \mu = 0.094$
	$R = 5.0\ mm : \mu = 0.098$
	$R = 7.5\ mm : \mu = 0.080$
	$R = 10\ mm : \mu = 0.078$
	All other radii: $\mu = 0.086$
Punch velocity	$v_p = 1.365\ mm/s$
Maximum time increment	$\Delta t_{max} = 0.05\ s$
Flow curve	Combined Hockett-Sherby/Gosh
Yield locus	Hill 48
Hardening law	Isotropic hardening
Flow rule	Associated flow rule

Experimental verification via force displacement curves

Figure 7 shows simulated force displacement curves together with an average over three repetitions of the experimental force displacement curves until fracture. Both the slope before and the slope after the force maximum are in good agreement with the experimental data. Since the slopes after the force maximum are well matched in both simulation and experiments, the mesh size is considered to be fine enough to capture the effect of localization.

Experimental verification via thicknesses along the neck

Nine thickness measurements along the neck of the samples that forms at the punch apex were taken with a point micrometer and were compared to simulation thicknesses at the same punch displacements shortly before fracture. The measurements validate the plasticity model in terms of r-values, which is responsible for both thinning and the strain rate sensitivity, which translates into homogenized strains and therefore delays localization. Figure 8 shows the comparison of thickness measurements along the width of the sample for each of the experimental punch radii. Both the form and the thickness of the virtual samples along their neck match the experimental data. Since the experimental samples were cut with wire EDM and not
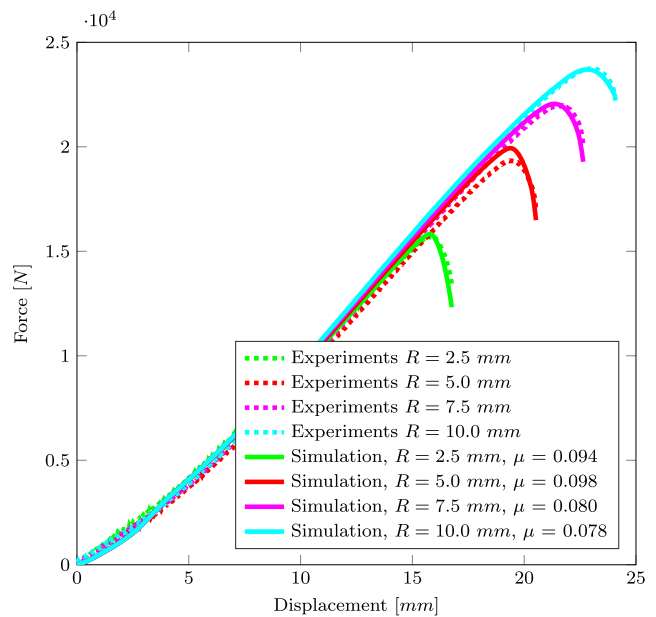

Fig. 7 Experimental and simulation force displacement curves for DP600 sheet steels undergoing angular stretch bending with 2.5, 5.0, 7.5, and 10 mm punch radii
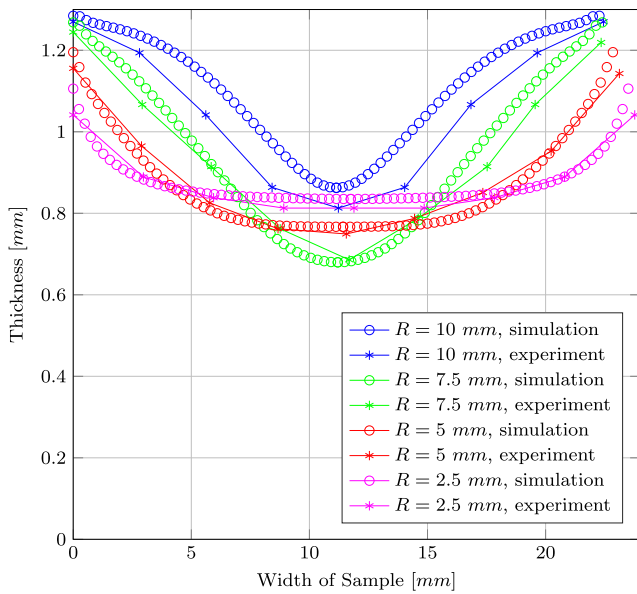
Fig. 8 Comparison of experimental and simulation thickness measurements along the localized neck

sheared, fracture starts in the inside and propagates to the edges (as predicted by the simulation). Therefore, the plasticity model is considered to be accurate and the extraction of strains in the simulation close to the force maximum are considered to be valid.

The time-dependent method

Forming limit diagrams signal the onset of localized necking for given major and minor strains in sheet metal forming. However, the localization in strains, and therefore the localized neck, is not a discrete state that suddenly follows the diffuse neck. The localization is continuously developed through the decreasing size of the diffuse neck. The forming limit strains can be defined in many ways. A frequently-used mathematical description is the modified maximum force criteria by Hora et al. [2], which extends the maximum force criteria to access localized necking strains by incorporating the stabilizing rise in stresses as the stress state moves from uniaxial to plane strain. The most used experimental technique to access localized necking strains is the Nakazima test, where dog-bone-shaped samples with increasing width (to vary the strain paths from uniaxial to biaxial) are drawn into a die by a spherical punch. The strains on the top surface of the sheet are recorded and evaluated by different techniques, which define the localized necking strains. A newly introduced technique to define the localized necking strains in a Nakazima test is the so-called time dependent method that was introduced by Volk and Hora, which has been adopted for accessing the localized necking strains in
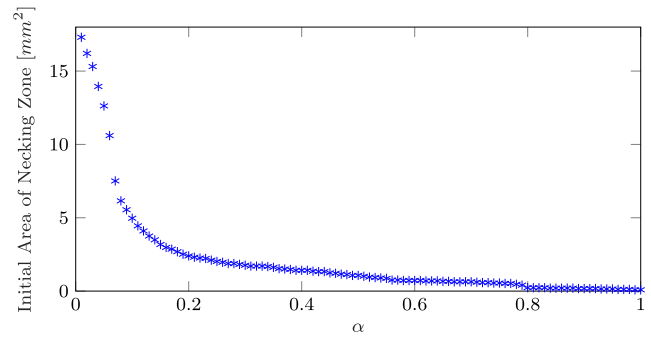

Fig. 9 α versus initial area of necking zone, $R = 7.5\ mm$

the angular stretch bend test. A more detailed derivation of the following equations can be found in Volk and Hora's publication on the time-dependent method [14].

The time-dependent method makes use of the local concentration of strains in the instability zone until fracture occurs and the surrounding areas fall back into the elastic range. Therefore, strains inside the instability zone increase, while other areas remain at a constant strain. To amplify this effect, thinning rates are used to identify the last stable state. Thinning rates inside the localization zone increase rapidly, while thinning rates outside the localization zone return to zero. The algorithm is defined in three steps.

Identification of the necking area The identification of the elements that are in the necking zone is accomplished by calculating the representative maximum thinning rate $\bar{\dot{\epsilon}}_{max}$, which is defined as the arithmetic mean value of the five highest thinning rates in the second-to-last time step.

$$\bar{\dot{\epsilon}}_{max} = \frac{1}{5} \sum_{i=g-4}^{i=g} \dot{\epsilon}_i^{b-1} \qquad (6)$$

Every element with a thinning rate higher than $\alpha \bar{\dot{\epsilon}}_{max}$ in the second-to-last time step is then identified as an element in the necking zone. N is the union of these elements and n is the number of elements in N.

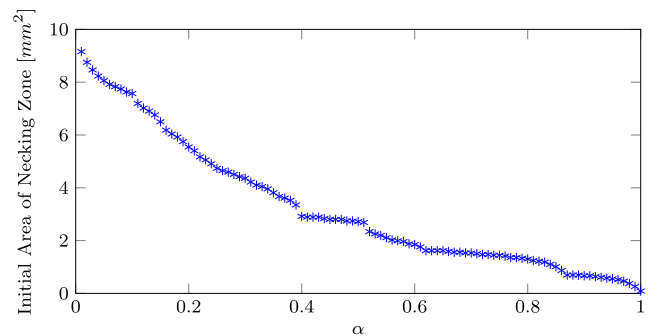$$N = all\ elements\ with\ \dot{\epsilon}_i^{b-1} \geq \bar{\dot{\epsilon}}_{max} \qquad (7)$$

Fig. 10 α versus initial area of necking zone, $R = 3\ mm$

Table 5 Values for α for all punch radii

R [mm]	2.0	2.25	2.5	2.75	3.0	3.5	4.0	4.5	5.0	7.5	10.0	12.0	13.0	38.0
α	0.95	0.98	0.98	0.99	0.95	0.95	0.95	0.95	0.9	0.75	0.75	0.7	0.6	0.3

The value of α is chosen so that the initial area of the necking zone is saturated and does not vary for small changes in α. Figures 9 and 10 show the dependency of the initial necking area on α. For the 7.5 mm punch radius, α is chosen 0.6, and for the 3.0 mm punch radius, α is chosen 0.95, in order to obtain a stable necking area.

Table 5 shows all α values for their associated punch radii.

Identification of beginning instability The representative thinning rate of $\bar{\dot{\epsilon}}_{rep}^{k}$ is defined as arithmetic mean value of the thinning rates of all elements in the necking zone for every time step k.

$$\bar{\dot{\epsilon}}_{rep}^{k} = \frac{1}{n} \sum_{i=1}^{i=n} \dot{\epsilon}_i^k, \; for \; all \; elements \; in \; N \tag{8}$$

Figure 11 shows the identification of the last stable time increment, along with the representative thinning rate for the angular stretch bend test simulation at a 7.5 mm radius. Two characteristic regions arise: a linear increase with low slope at the beginning standing for homogeneous deformation and a linear increase with high slope at the end standing for localized unstable deformation, while a curved region occurs in between these two. The two linear regions are used
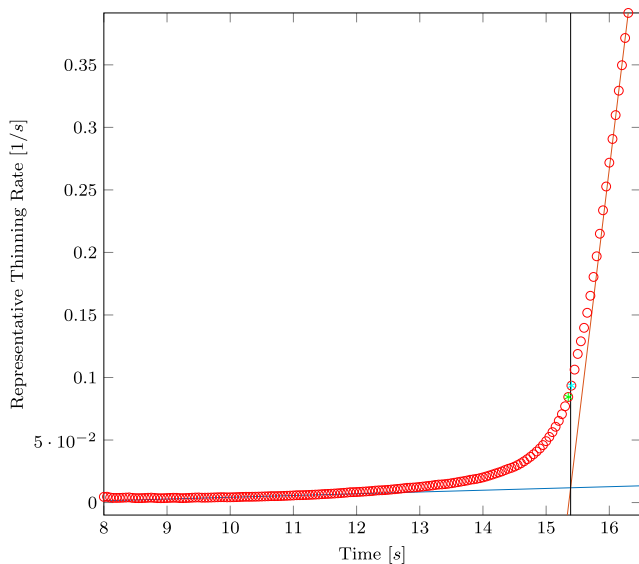
to define the last stable time step before instability. A sequence of linear curve fitting is applied to find the two best linear fits through the two linear regions of the representative thinning rate. The intersection of these lines gives the transition point from stable to unstable, and the last time step before the intersection is considered to be the last stable time step.

Calculation of strain values at the point of instability The mean value of the principal strains ϵ_1^{stab} and ϵ_2^{stab} of all elements in the necking zone give the localized necking strains as

$$\epsilon_1^{LN} = \frac{1}{n} \sum_{i=1}^{i=n} \epsilon_{1,i}^{k_{stab}}, \; for \; all \; elements \; in \; N \tag{9}$$

$$\epsilon_2^{LN} = \frac{1}{n} \sum_{i=1}^{i=n} \epsilon_{2,i}^{k_{stab}}, \; for \; all \; elements \; in \; N \tag{10}$$

The finite element model of the angular stretch bend test consists of fifteen layers through the thickness of the sample. Considering that strains are higher on the convex side of the sheet, the thinning rates are extracted at the outmost layer on the convex side, which is where the necking area (and therefore the area of analysis) should occur.
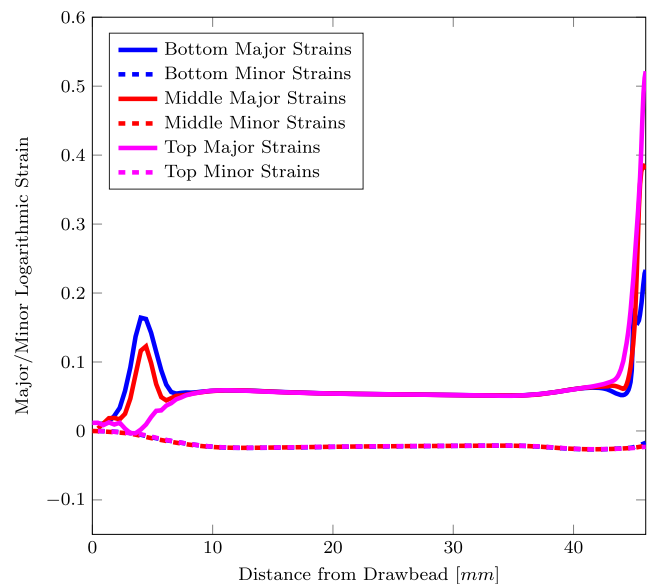

Fig. 11 Last stable and first unstable time increments, as identified through implementation of the time-dependent method and the 7.5 mm punch radius

Fig. 12 Ligament minor and major strains for bottom, middle, and top layers for $R = 2.5 \; mm$ at the last stable time increment

Fig. 13 Sheet of the 2.5 mm punch radius at the last stable time increment. High strains are reached on the convex side of the sheet due to the constraining concave side of the sheet. A deep valley is built
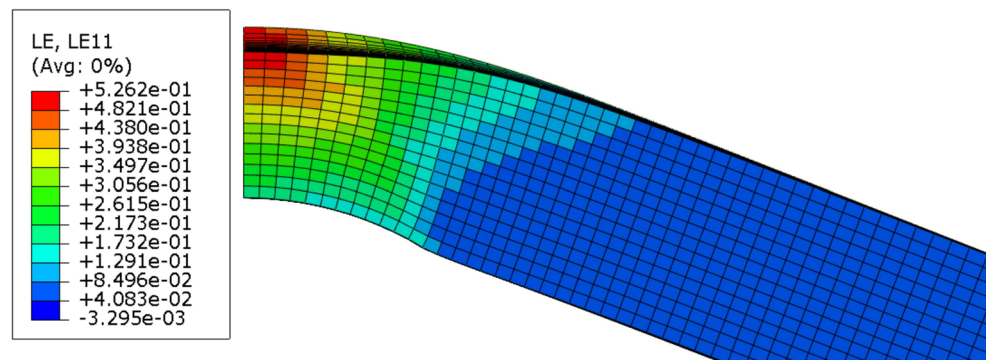
Results

Major and minor strains along the ligament Major and minor strains are extracted along the center line of the sheet at the top surface (the convex side of the sheet), the middle surface, and the bottom surface (the concave side of the sheet) at the last stable time increment. Figure 12 shows the major and minor logarithmic strains at the onset of localized necking, predicted by the time-dependent method for the 2.5 mm radius. The major strains vary at a displacement from the draw bead of about 5 mm, and at the punch nose at approx. 46 mm from the draw bead. This variation is due to the left bend of the sample at the die entry radius and the right bend at the punch nose. When examining the major strains on the right side of the plot, it is obvious that the ones on the top surface are highest, since the bending component superimposes the highest tension to the stretching component, followed by the mid-surface major strains, and finally the bottom surface major strains. A plane-strain condition is reached at the punch nose because the minor strains are almost zero at a displacement from the draw bead of 46 mm.

Figures 13, 14, 15 and 16 illustrate simulated sheets that are stretched and bent by different radii. The sheets are dissected along their center plane. The smaller the radius, the

more pronounced, local, and delayed is the valley that forms during the localization procedure. This condition originates from the lower sheet layers, which are able to constrain the convex necking layer. The higher the bending, the higher the constraints; and therefore, the deeper the valley before instability.

Influence of the bending component on the FLD_0 value The observations in strains along the ligament of the samples will now be used to derive an analytical relationship of the bending component on the forming limits in plane strain of a sheet. In order to obtain a comparable measure of the forming limits with superimposed bending, the mid-plane strains at the punch apex in the last stable time increment of each sample will be considered to be the forming limits. Furthermore, the mid-plane minor and major strains are transformed to major strains only with a slope of -1 in the $(\epsilon_{min}, \epsilon_{maj})$ space (see Fig. 17). This transformation is done in correspondence to the form of the Keeler-Brazier forming limit curve (see Eqs. 12–14), which will later be extended with a third axis.

As a measure of the bending component, a thickness over radius ratio of t/R for the different radii was used. Next, the FLD_0 values were plotted over their respective t/R ratios and an empirical analytical relationship between the t/R

Fig. 14 Sheet of the 4 mm punch radius at the last stable time increment. The smaller the bending component, the smaller the strains at the onset of instability and the smaller the valley that is built during stretch bending
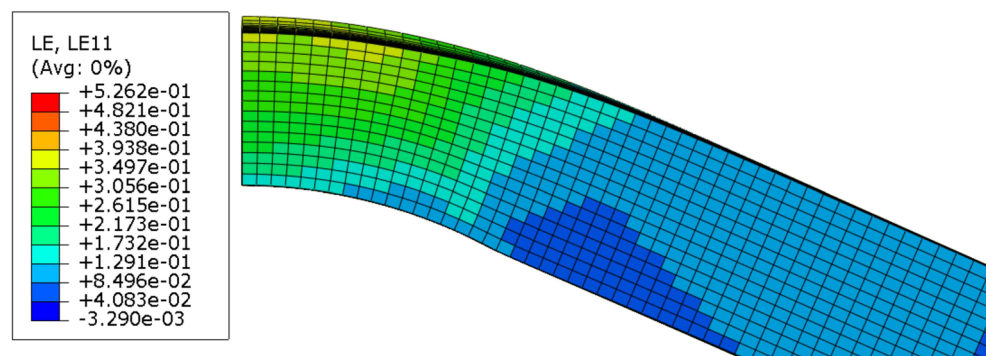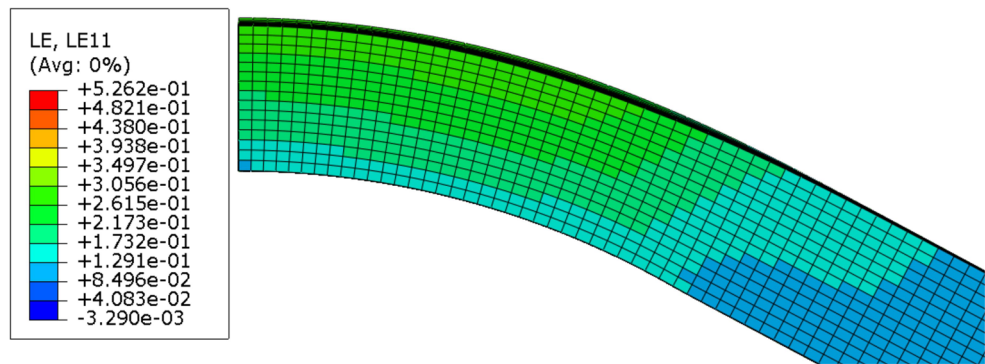
Fig. 15 Sheet of the 7.5 *mm* punch radius at the last stable time increment. The strain gradient through the thickness of the sheet is decreasing with the superimposed bending component

ratios and the FLD_0 values for different bending radii was fitted through the data points (see Fig. 18 and Eq. 11).

$$FLD_0\left(\frac{t}{R}\right) = FLD_{0,noBending} + A\left(\frac{t}{R}\right)^n \qquad (11)$$

The first term in Eq. 11 stands for the forming limit in plane strain for no superimposed bending, and is therefore the y-intercept in Fig. 18. The second term captures the mechanics that occur on the top surface when bending is superimposed, which result in enhanced formability. The forming limit strains of the top surface increase with an increasing bending component, times a value A and to the power of a value n. The higher the bending component, the more the top surface is constrained by the deformation of lower surfaces. Therefore, the top surface instability is delayed because the deformation underneath the top surface is pulling in the opposite direction, and the forming limit strains increase as a result. The values for $FLD_{0,noBending}$, A and n are listed in Table 6.

Extended forming limit diagram after Keeler-Brazier The Keeler-Brazier forming limit diagram [1] is now extended by a third axis: the superimposed bending component t/R.

The original empirical equations consist of a forming limit in plane strain, FLD_0 (Eq. 12), which is dependent on the strain-hardening exponent n in the Hollomon hardening law and the initial sheet thickness t_0. The left side of the forming limit diagram decreases linearly with ϵ_{min} (Eq. 13), while the right side increases as a function of a logarithm that depends on the values of $FLD_{0,KB}$ and ϵ_{min} (Eq. 14).

$$FLD_{0,KB} = \ln\left[1 + \frac{23.3 + 14.14t_0}{100}\left(\frac{n}{0.21}\right)\right] \qquad (12)$$

$$\epsilon_{maj} = FLD_{0,KB} - \epsilon_{min}, \ \epsilon_{min} \leq 0 \qquad (13)$$

$$\epsilon_{maj} = \ln\left[0.6(e^{\epsilon_{min}} - 1) + e^{FLD_{0,KB}}\right], \ \epsilon_{min} > 0 \qquad (14)$$

In the extended version of the Keeler-Brazier FLD, the $FLD_{0,KB}$ value is substituted by the bending dependent $FLD_0\left(\frac{t}{R}\right)$ under the assumption that the enhanced formability in plane strain due to bending has equal influence in both the uniaxial and biaxial regions. Although this assumption may not be always true, it provides a starting point for the effect of bending on the FLD for strain paths other than plane strain. Figure 19 shows the extended three-dimensional forming limit diagram.

Fig. 16 Sheet of the 10 *mm* punch radius at the last stable time increment. Almost no valley is built during the stretch bending process for large radii. Strains at the onset of localized necking are close to the strains without any superimposed bending
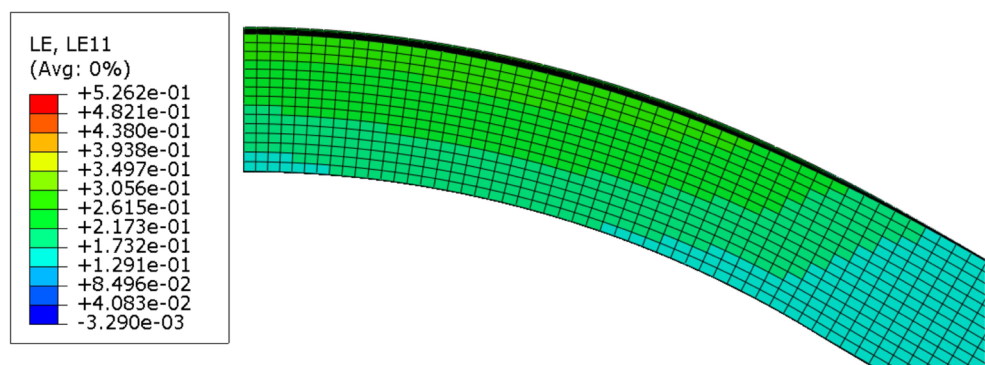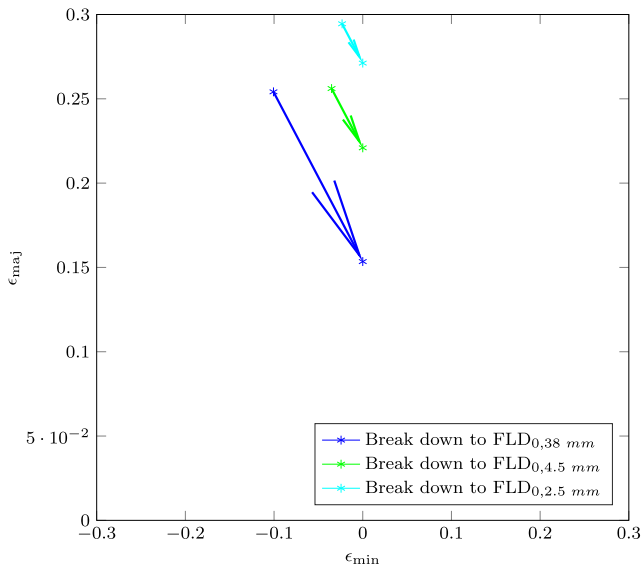
Fig. 17 Breakdown of extracted forming limits of mid-planes for 38, 4.5 and 2.5 *mm* with a slope of − 1 to major strains only
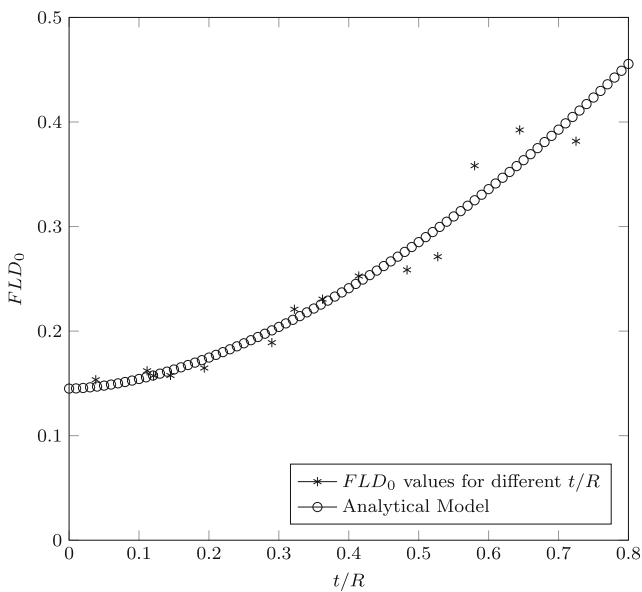

Fig. 18 Analytical model that describes the enhanced formability, due to bending in plane strain fitted through the data points

Table 6 Fitted parameters for the analytical model

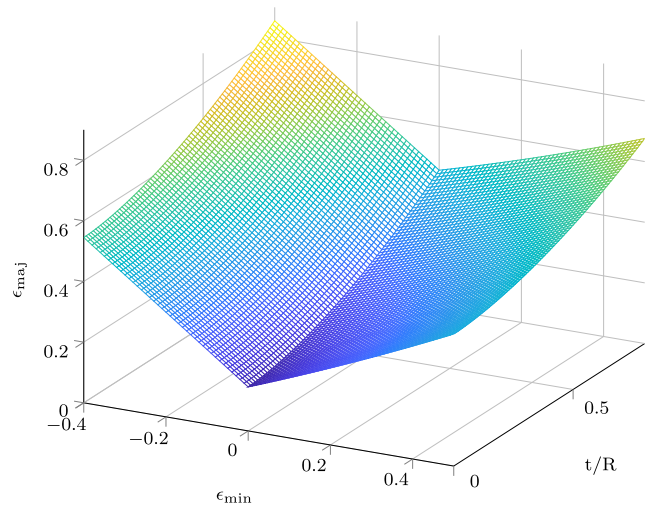| $FLD_{0,noBending}$	A	n
0.15	0.45	1.70

Fig. 19 Keeler Brazier FLD extended by a superimposed bending axis

Conclusions

Our proposed methodology enables the quantitative assessment of the formability of sheet metals that are subjected to stretching with superimposed bending. To enable such an analysis, numerical simulations of an angular stretch bend test are deployed to subject a sheet steel to tension with different amounts of superimposed bending. A time-dependent method is implemented to assess localized necking strains in our simulations. The forming limits for different stretch-bending states are then used to calculate an analytical dependency of the forming limit on the bending component. As an example, this analytical relation is used to extend the FLD after Keeler-Brazier, but can be used to extend any other FLD.

The methodology was shown for a DP600 sheet steel that has been tested and characterized using tensile tests in different directions to the rolling direction and at different strain rates. The constitutive model fitted for the DP600 steel consists of a mixed Hockett-Sherby/Gosh flow curve with strain rate dependency, after Johnson-Cook. The anisotropy is modeled using a Hill 48 yield locus with isotropic hardening and an associated flow rule.

Verifications of the model in terms of force displacement curves and thickness measurements along the width of the sample emphasize the validity of the simulation, and therefore suggest that numerical experiments are sufficient to extend a forming limit diagram. For the DP600 steel tested in our experiments, its formability is enhanced by factor 3 for plain strain and a thickness-over-radius ratio of 0.8.

Compliance with Ethical Standards

References

1. Keeler SP, Brazier WG (1975) Relationship between laboratory material characterization and press-shop formability
2. Hora P, Tong L, Berisha B (2013) Modified maximum force criterion, a model for the theoretical prediction of forming limit curves. Int J Mater Form 6(2):267–279
3. Tharrett MR, Stoughton TB (2003) Stretch-bend forming limits of 1008 AK steel
4. Kitting D, Koplenig M, Ofenheimer A, Pauli H, Till ET (2009) Application of a "Concave-Side Rule" approach for assessing formability of stretch-bent steel sheets. Int J Mater Form 2(1):427–430
5. Neuhauser FM, Terrazas OR, Manopulo N, Hora P, Van Tyne CJ (2016) Stretch bending - the plane within the sheet where strains reach the forming limit curve. In: IOP Conference series: Materials science and engineering, vol 159
6. Kitting D, Ofenheimer A, Pauli H, Till ET (2010) A phenomenological concept to predict formability in stretch-bending forming operations. Int J Mater Form 3(1):1163–1166
7. Kitting D, Ofenheimer A, Pauli H, Till ET (2011) Experimental characterization of stretch-bending formability of ahss sheets. AIP Conference Proceedings 1353(1):1589–1594
8. Levy BS, Van Tyne CJ (2009) Predicting breakage on a die radius with a straight bend axis during sheet forming. J Mater Process Technol 209(4):2038–2046
9. de Kruijf NE, Peerlings RHJ, Geers MGD (2009) An analysis of sheet necking under combined stretching and bending. Int J Mater Form 2(1):845–848
10. Xia C, Zeng D (2008) Sheet metal forming limit under stretch-bending. In: Proceedings of the 2008 International Manufacturing Science and Engineering Conference, pp 1–7
11. Vallellano C, Morales D, Martinez AJ, Garcia-Lomas FJ (2010) On the use of concave-side rule and critical-distance methods to predict the influence of bending on sheet-metal formability. Int J Mater Form 3(1):1167–1170
12. Morales-Palma D, Vallellano C, García-Lomas FJ (2013) Assessment of the effect of the through-thickness strain/stress gradient on the formability of stretch-bend metal sheets. Mater Des 50:798–809
13. Hora P, Tong L (2008) Theoretical prediction of the influence of curvature and thickness on the enhanced modified maximum force criterion. Numisheet 7:205–210
14. Volk W, Hora P (2011) New algorithm for a robust user-independent evaluation of beginning instability for the experimental FLC determination. Int J Mater Form 4(3):339–346